Growth interactions between icosahedral quasicrystals

Nancy Senabulya* and Ashwin J. Shahani†
Department of Materials Science and Engineering, University of Michigan, Ann Arbor, Michigan 48109, USA

(Received 10 July 2019; published 11 September 2019)

We investigate the solidification pathways of a population of icosahedral quasicrystals in a liquid through *in situ* synchrotron x-ray tomography. The wealth of three-dimensional space- and time-resolved data enables us to test the predictions of various models and theories of crystallization on a quasi-crystal-forming alloy. Remarkably, we find the general evolution equation—that accounts for the competing effects of growth, coalescence, and coarsening—fits well our experimental data on surface area concentration. Furthermore, we quantify the orientation selection, screening length, and coarsening rate of the dodecahedra, and compare these results to that of periodic crystals. The latter is a full order of magnitude smaller than that of elemental metal dendrites in the limit of zero volume fraction, a reflection of the low solid-liquid interfacial energy of the icosahedral phase. Our paper provides the critical input data for microstructural models used for integrated computational materials engineering of complex intermetallics, including quasicrystals.

DOI: 10.1103/PhysRevMaterials.3.093403

I. INTRODUCTION

Quasicrystals (QCs) possess long-range positional order but noncrystallographic orientational order, e.g., 5-, 8-, 10-, and 12-fold symmetries. Despite their frequent observation in both metallic alloys [1–3] and soft matter structures [4–6] in the 35 years since their discovery [7,8], little is known about the way they emerge from the melt. For this reason, Steurer has recently identified the problem of QC growth as one of the open questions in the field [9]. For instance, is the growth process of QCs limited by the localized *attachment* of such atoms or clusters [10–12] to the growth front, or rather the long-range *transport* of these entities within the melt?

The vast majority of experiments suggest that QCs grow by the forward advancement of facets. Evidence comes from *post mortem* observations of microvoids within QCs (so-called "negative" QCs), which show a fully faceted morphology [13,14]. Yet such voids are bounded by a liquid-gas interface, and thus, the kinetic processes leading to their formation might not be representative of what happens during the liquid-to-solid transition. Other studies make detailed assessments based on the external surfaces of quenched specimens (e.g., Refs. [15–17]), yet this approach is somewhat unreliable due to the continued crystal growth that occurs during the quenching process. In other words, it is impossible to reconstruct the dynamical events that led to the formation of QC grains that can extend up to the centimeter size, see Ref. [3] for a review. To this end, a few investigators have studied QC solidification through real-time x-ray imaging [18–22]. In particular, Senabulya *et al.* have employed synchrotron-based x-ray microtomography (XRT) to capture the growth and relaxation of a *single* icosahedral QC (denoted as *i*-QC) in three-dimensional (3D) space and in time [21]. Their four-dimensional measurements point to the dominance of bulk transport over interfacial processes; they also show that the growth shape of the *i*-QC is a pentagonal dodecahedron, consistent with theoretical predictions. We pick up where this study had left off, by considering a *collection* of *i*-QCs undergoing solidification and evaluating the degree of interaction between them. As in that work, our investigation is made possible due to developments in computational tools to extract meaningful information from the high-dimensional data.

Put more rigorously, the present paper is aimed at answering two main questions: The first is, how well do volume-averaged models of crystallization describe the evolution of polyhedral particles, in this case QCs? Such models have been traditionally employed to understand the evolution of dendritic alloys during growth and coarsening. Yet dendrites and polyhedra are obviously morphologically dissimilar. The second is, how do the nucleation, growth, and coarsening behaviors of quasicrystals compare to periodic crystals, such as metallic dendrites? The answer to this question hinges on the answer to the first, i.e., the suitability of the models (described below) in capturing the microstructural dynamics. By achieving these two goals, we can place icosahedral quasicrystals on the same plane of analysis as their periodic counterparts, at least, in terms of kinetic properties.

II. METHODS

The experimental methods employed in this paper largely follow that of Ref. [21]. Master alloy samples of composition $Al_{74}Pd_{20}Mn_6$ were prepared *via* vacuum arc-remelting using high-purity elemental Al (99.999% purity), Pd (99.9% purity) and Mn (99.9% purity) at the Materials Preparation Center at Ames National Laboratory in Ames, Iowa. The cast alloy buttons were cut into cylinders of 1-mm diameter by 5-mm height for the XRT experiment. The sample rod was further thinned mechanically to ~400 μm to increase

*Present address: Michigan Center for Materials Characterization, University of Michigan, Ann Arbor, Michigan 48109.
†shahani@umich.edu

x-ray transmission. The synchrotron XRT experiment was conducted at beam-line 2-BM of the Advanced Photon Source at Argonne National Laboratory in Lemont, Illinois. The cylindrical samples were inserted into an x-ray transparent boron nitride sample holder, which was, subsequently, placed inside a resistive furnace at the beam line. The assembly was first heated for 5 min at 915 °C, which is well above the liquidus temperature of the *i*-QC phase; this was performed so as to homogenize the melt. Then, the sample was cooled from 915 °C to 875 °C at a rate of 1°/min thereby promoting the formation of *i*-QCs from the parent liquid. During the cooling segment, x-ray projection images were collected continuously at a rate of 50 Hz and sample rotation speed of 6°/s, resulting in 1500 projections evenly spaced between 0° and 180° and a temporal resolution of 30 s between subsequent tomograms. We use a polychromatic "pink" beam centered at 27 keV and a PCO Edge 5.5 complementary metal-oxide semiconductor camera optically coupled to a 20-mm-thick LuAg:Ce scintillator for data collection. The field of view (FOV) on the detector plane measured 2560 × 1200 pixels with a pixel size of 0.652^2 μm^2. Based on our prior experience, these parameters enable us to monitor the solidification dynamics at sufficiently high spatial and temporal resolutions [21].

Following the experiment, the XRT data was passed through TOMOPY, a Python-based open-source framework for tomographic data processing [23]. Within TOMOPY, we normalize projection images, remove "ring" artifacts, and reconstruct the data; see Ref. [21] and the references therein for further details. Further data processing was performed using the Image Processing toolbox in MATLAB R2016B [24]. In MATLAB, the reconstruction images were filtered and segmented into solid QC and liquid phases, allowing for precise determination of QC volume fraction and surface area as solidification proceeds. The solid-liquid interfaces were also meshed, or represented as a series of triangles and vertices. We smoothed the meshed structure through mean curvature flow [25] in order to remove any "staircasing" artifacts that result from the marching-cubes meshing procedure. The resulting mesh face and vertex positions are used to quantify the local interfacial structure and its dynamics. More specifically, the orientation (interface normal) $\hat{n}$ of a given mesh triangle is given by the curl of its edge vectors, and the velocity v is calculated using a nearest-neighbor approach [21,26,27]. Following thermodynamic convention, $\hat{n}$ points from QC to liquid and positive v correspond to growth, and negative v corresponds to dissolution.

III. RESULTS AND DISCUSSION

A. Three-dimensional views of QC solidification

The growth process is shown in Fig. 1. We capture three QCs within the FOV. The first QC (top) nucleates heterogeneously on the oxide skin (translucent gray) at 904.5 °C, followed by the second QC (bottom left) at 904 °C, and a third (bottom right) at 903.5 °C. We denote the time at which the first appears as the origin of our time axis such that all reported times (below) are relative to this reference state. We also specify the specimen frame of reference such that the $\hat{z}$ axis is along the rotation axis of our sample. The solid-liquid

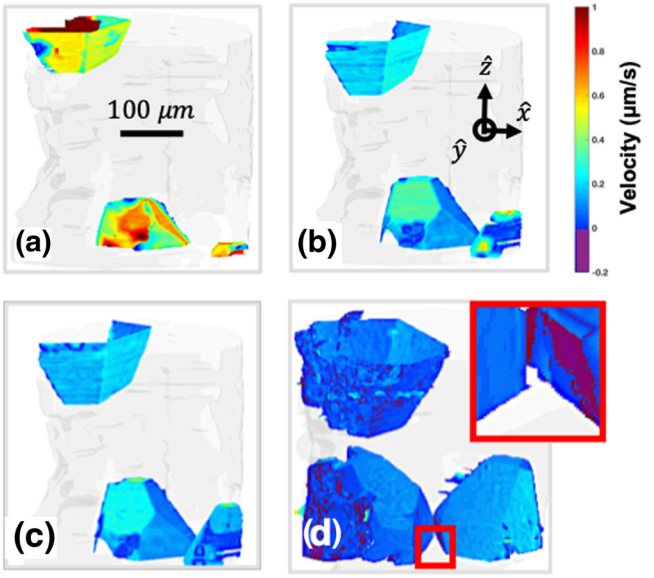

FIG. 1. *Three-dimensional reconstructions of quasicrystal growth* at (a)–(d) 60 s (903.5 °C), 120 s (902.5 °C), 480s (896.5 °C), and 540 s (895.5 °C), respectively, following nucleation at 0 s (904.5 °C). QC-liquid interfaces are colored according to the facet normal velocity. The oxide skin (Al_2O_3) is rendered translucent gray. The inset in (d) shows a zoom in of colliding facets between neighboring QCs. The smaller of the two QCs has a facet with negative velocity, indicating dissolution.

interfaces are colored according to interface velocity: Positive velocities are mapped onto a blue-cyan-yellow-red color map whereas negative velocities are rendered purple. The plotted velocities tend to decay over time due to the depletion of solute in the liquid phase as the QCs grow [21], varying from as high as 1 μm/s following nucleation to near zero at the later stages of solidification. In fact, one facet shows negative velocities when it approaches a neighboring QC at long times, see the inset in Fig. 1(d). Diffusional interactions between the two QCs trigger dissolution of this particular facet. Below, we analyze in greater detail the different stages of QC solidification from nucleation and growth to coarsening and coalescence.

B. Orientation selection of quasicrystalline nuclei

Figure 2(a) shows stereographic projections of solid-liquid interfacial normals of the three QCs that nucleate heterogeneously from the oxide skin of the sample into the liquid. Peaks in the distributions specify the locations of the QC facets. Interestingly, all three dodecahedral particles have different orientations. From left to right, one nucleates with its fivefold axis parallel to the specimen $\hat{z}$ direction [cf. Fig. 1(a)], the second with its twofold axis parallel to $\hat{z}$, and the last with its threefold axis parallel to $\hat{z}$. See also the inset in Fig. 2(b) for a schematic. Note that the third peak in the rightmost stereographic projection appears to be "missing," yet this is due to the fact that the oxide occludes some of the crystal surfaces.

To understand better the diversity in QC orientation, we turn to the QC-oxide interfacial free energy, denoted as γ_{wc}.

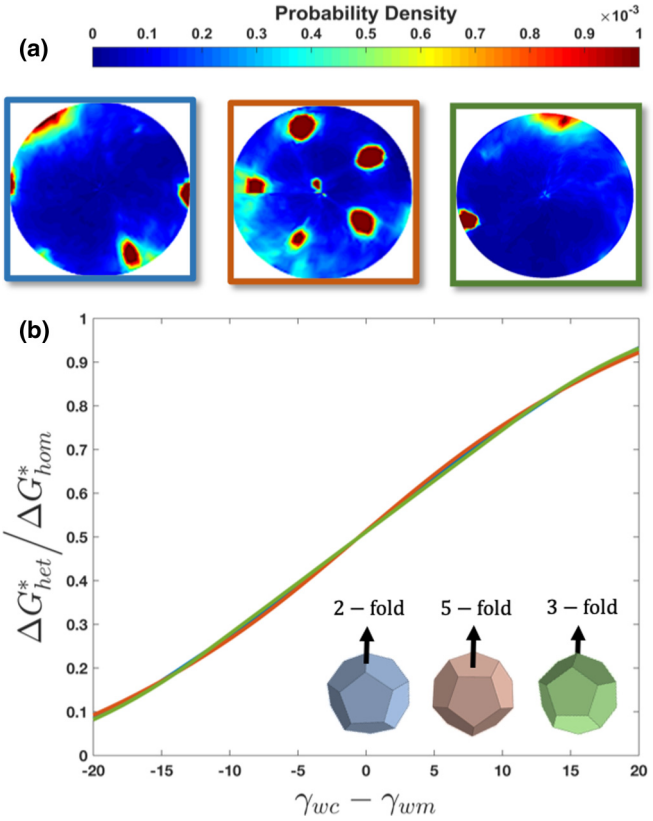

FIG. 2. *Orientations of nucleated quasicrystals*. (a) Stereographic projections of solid-liquid interfacial orientations of three QCs that nucleate within the tomographic region of interest. The zone axis in all cases corresponds to the specimen $\hat{z}$ (upper) direction of the experiment (see Fig. 1). One QC is oriented with its twofold axis $\| \hat{z}$, the second is oriented with its fivefold axis $\| \hat{z}$, and the third is oriented with its threefold axis $\| \hat{z}$. (b) Calculations of Gibbs free energy upon heterogeneous nucleation as a function of interfacial energy. The colors indicate the upper direction of the nucleated crystals, see the inset.

Uwaha [28] and Taylor and Cahn [29] have pointed out that, for an anisotropic particle, certain orientation relationships between the particle and the substrate can be energetically preferred. For instance, Fujiwara *et al.* have demonstrated that, in the case of an octahedral Si particle on an inert substrate, the ⟨100⟩ or ⟨111⟩ upper directions (i.e., parallel to the substrate) are stable [30]. Since the total free energy scales with the crystal volume for a given crystallization driving force, the particle will change its orientation in order to reduce the volume as the interfacial tension changes. That is, the heterogeneous nucleation barrier ΔG^*_{het} is directly proportional to nucleus volume V_c^* with a specific orientation [28,29]. According to the Winterbottom construction [31] or the Wulff-Kaischew theorem [32], the volume V_c^* itself is related to the "wetting strength" $\gamma_{wc} - \gamma_{wm}$ where γ_{wm} is the oxide-melt interfacial free energy. Since interfacial energies are difficult to measure experimentally, we plot in Fig. 2(b) the nucleation barrier against the wetting strength as a function of QC orientation [corresponding to the three cases in Fig. 2(a), see the Appendix for computational details]. In the limit the wetting strength is large and negative, the crystal volume and nucleation barrier are both zero; heterogeneous nucleation cannot occur. In the opposite extreme, the entire dodecahedron lies above the oxide surface, and the QC nucleates homogenously in the melt with an associated barrier ΔG^*_{hom}. Thus, $0 \leqslant \Delta G^*_{\text{het}}/\Delta G^*_{\text{hom}} \leqslant 1$. It is clear from Fig. 2(b) that there is very little difference among the three orientations, unlike the Si particles mentioned earlier which show a significant difference in $\Delta G^*_{\text{het}}/\Delta G^*_{\text{hom}}$ (on the order of ± 0.1 [30]) with respect to crystal orientation. This would explain why all three QC orientations are equally probable upon heterogeneous nucleation. The plot also suggests that it is impossible to select a substrate with appropriate interfacial energy γ_{wm} so as to control the orientation of QC nuclei, a serious implication for the manufacture of QC materials. Geometrically, a dodecahedron (with 20 vertices) is closer to a sphere (infinite vertices) compared to an octohedron (six vertices). Therefore, changes in nucleus volume and the corresponding nucleation barrier are less sensitive to changes in orientation for a fixed volume. Since QCs are known to possess highly faceted Wulff shapes (which contain many such vertices) [13,14,21], these results are generalizable.

C. Macroscopic statistics on quasicrystal growth

Once nucleated, the crystals grow by mass diffusion and consume the supersaturation. The volume fraction $g = V_c/V$ rises wherein V_c is the QC volume following nucleation (i.e., $V_c \geqslant V_c^*$) and V is the sample volume. Concomitant with an increase in g is an increase in the interfacial area concentration S, especially at the early stages of the growth process. We define S as A_{cm}/V where A_{cm} is the crystal-melt interfacial area. The reciprocal of this quantity has units of length and represents an important integral measure of the overall length scale of the microstructure during alloy solidification [33]. Importantly, S does not continue to rise indefinitely as g approaches unity. At high volume fractions, particles interact with each other *via* soft collisions (i.e., overlapping diffusion fields) [34,35] and "hard" collisions (i.e., impingements) [36]. Consequently, as the particles touch, there is a loss of free surface between them, and hence, the interfacial area concentration S drops. We quantify the evolution of g and S versus time and versus each other in Fig. 3. Errors arise from segmentation and further processing of the x-ray tomographic data. Both quantities increase monotonically but at a decreasing rate.

Neumann-Hyme *et al.* propose a general evolution equation for interfacial area concentration [37],

$$S = g(1-g)^r \left(S_0^{-3} + K_0 t\right)^{-1/3}, \tag{1}$$

where r, S_0, and K_0 are fitting parameters. The first term on the right-hand side accounts for uninterrupted growth, the second to interfacial coalescence, and the third to Ostwald ripening. The latter two terms contribute to a reduction in S and become increasingly important at high volume fractions g and long times t. Note that Eq. (1) combines the Cahn-Rath model of pure growth processes [38,39] $S \propto g^p(1-g)^r$ (where $p, r \in [0, 1]$) with the Lifshitz-Slyozov-Wagner (LSW) model of pure coarsening processes [40,41] $S = g(S_0^{-3} + Kt)^{-1/3}$ to obtain a comprehensive description of morphological evolution. Interestingly, the temporal exponent of $1/3$ has been found to be valid not only for isothermal coarsening, but

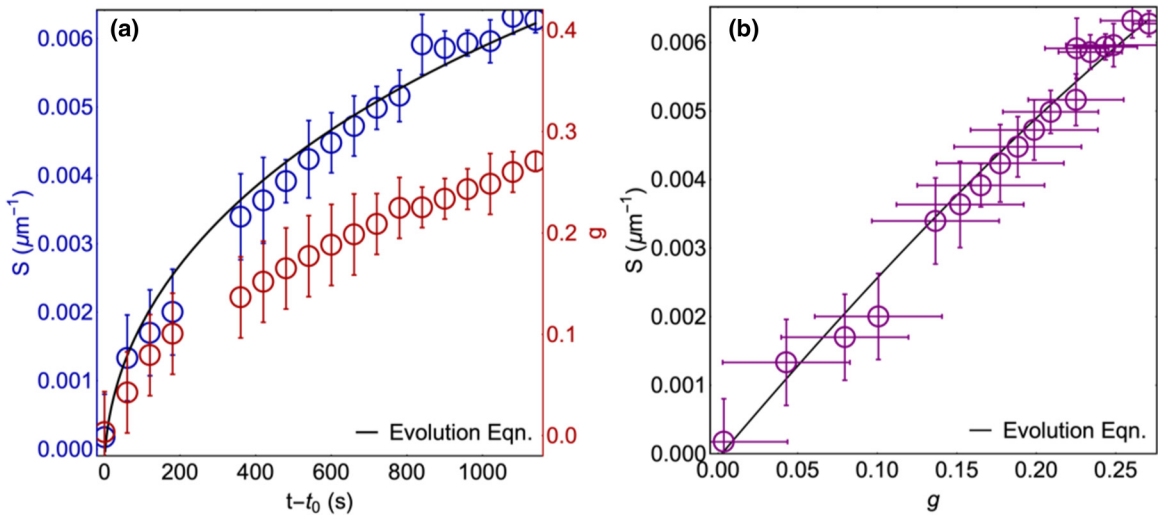

FIG. 3. *Macroscopic statistics of quasicrystal solidification*. (a) Time evolution of interfacial area density S and volume fraction g of a solid QC following nucleation at time t_0 and (b) S versus g. Volume V that is used to compute S is that of crystal plus liquid that is illuminated by the incident X radiation. Errors in the calculation of volume fractions and surface areas arise from segmentation and further processing of the x-ray tomographic data. The general evolution equation [Eq. (1), black lines] that accounts for growth, coalescence, and coarsening, fits well the experimental data.

also for concurrent growth and coarsening [42]. Equation (1) makes no assumption about the underlying morphology, so nothing precludes its application here. We fit our experimental data to the general evolution equation and obtain excellent agreement, see Fig. 3. The values of the fitting parameters are as follows: $r = 0.38$, $S_0^{-1} = 36.45\ \mu$m, and $K_0 = 3.97\ \mu\text{m}^3/\text{s}$. Although it is difficult at present to ascribe any specific meaning to the first two parameters, the last carries physical significance. Equating Eq. (1) with the LSW model shows that $K = K_0(1-g)^{-3r}$, and thus, K_0 is simply the coarsening rate constant in the limit of vanishing solid fraction. At finite volume fractions, $K > K_0$ since the interparticle distances become smaller and concentration gradients steeper. Comparing our data on QCs to that of simple metals dendrites (e.g., Al [43] and Mg [44]) reveals that the coarsening rate constant K_0 is about an order of magnitude smaller in our case. This result is somewhat surprising, especially in light of the higher temperatures involved in our experiment (~900 °C versus ~600 °C). As shown in Refs. [27,37,40,45], the coarsening rate constant varies proportionally with interdiffusivity as well as solid-liquid interfacial energy, among other thermodynamic properties. Holding all else constant, the extraordinarily low solid-liquid interfacial energy documented for QCs (~0.01 J/m^2 for the icosahedral phase [46] versus ~0.1 J/m^2 for Al [47] and Mg [48]) may contribute to a lower capillary driving force and, hence, the lower coarsening rate. The low interfacial energy of QCs arises from the icosahedral structural similarity between solid and undercooled melt [46]. Due to a lack of data, it is not possible at this stage to quantify the influence of interdiffusivity on the coarsening rate.

D. Local statistics on quasicrystal growth

For a closer glimpse on the QC interactions, we analyze the trajectories of all facets as a function of time. Figures 4(a) and 4(b) show the evolution of facet normal velocity, and Figs. 4(c) and 4(d) show the corresponding facet area for two QCs in the FOV. Consistent with Fig. 1, the velocity of all facets decays in time whereas, in general, the area increases. Discontinuities in the facet area are due to hard impingements between the two particles at ~700 s following nucleation (see the arrows). Even before coalescence, the QCs interfere with each other through soft collisions as mentioned above. According to Fig. 4(a), the onset of such diffusional interactions is ~300 s after nucleation. The facet velocities are nearly the same at this stage, but 60 s later, the velocity profiles diverge from one another. At the ~300-s mark, the nearest-neighbor distance between the two QCs is ~100 μm, indicating a diffusion Debye screening length of ~50 μm for each QC. This length scale determines the maximum range over which QC interactions occur, and beyond which such interactions cease [35]. In particular, the purple facet that is nearest to the other QC has a much lower velocity than all the others. As the two solid QCs grow toward each other, the concentration of the solute in the liquid decreases, and competitive growth or coarsening sets in. Eventually at ~600 s this same purple facet recedes [see negative velocity in Fig. 4(a)] at the expense of a growing orange facet on the opposing QC [see Fig. 4(b)].

To explain why one facet should fall back while the other propagates forward, we invoke the geometric evolution laws developed by Carter *et al.* [49] and Roosen and Carter [50]. They modeled the solid-liquid interface as a polygon having a limited number of allowed normal directions, all of which appear in the fully faceted Wulff shape. In this crystalline formulation, each interfacial facet f moves with some velocity v_f according to a linear kinetic law,

$$v_f = M(\hat{n}_f)[\langle\mu\rangle_f - \mu_{eq}(f)], \tag{2}$$

where $M(\hat{n}_f)$ is a mobility which depends on the facet orientation $\hat{n}_f$, $\langle\mu\rangle_f$ is the chemical potential in the liquid adjacent to the facet, and $\mu_{eq}(f) = \Gamma K$ is the equilibrium chemical

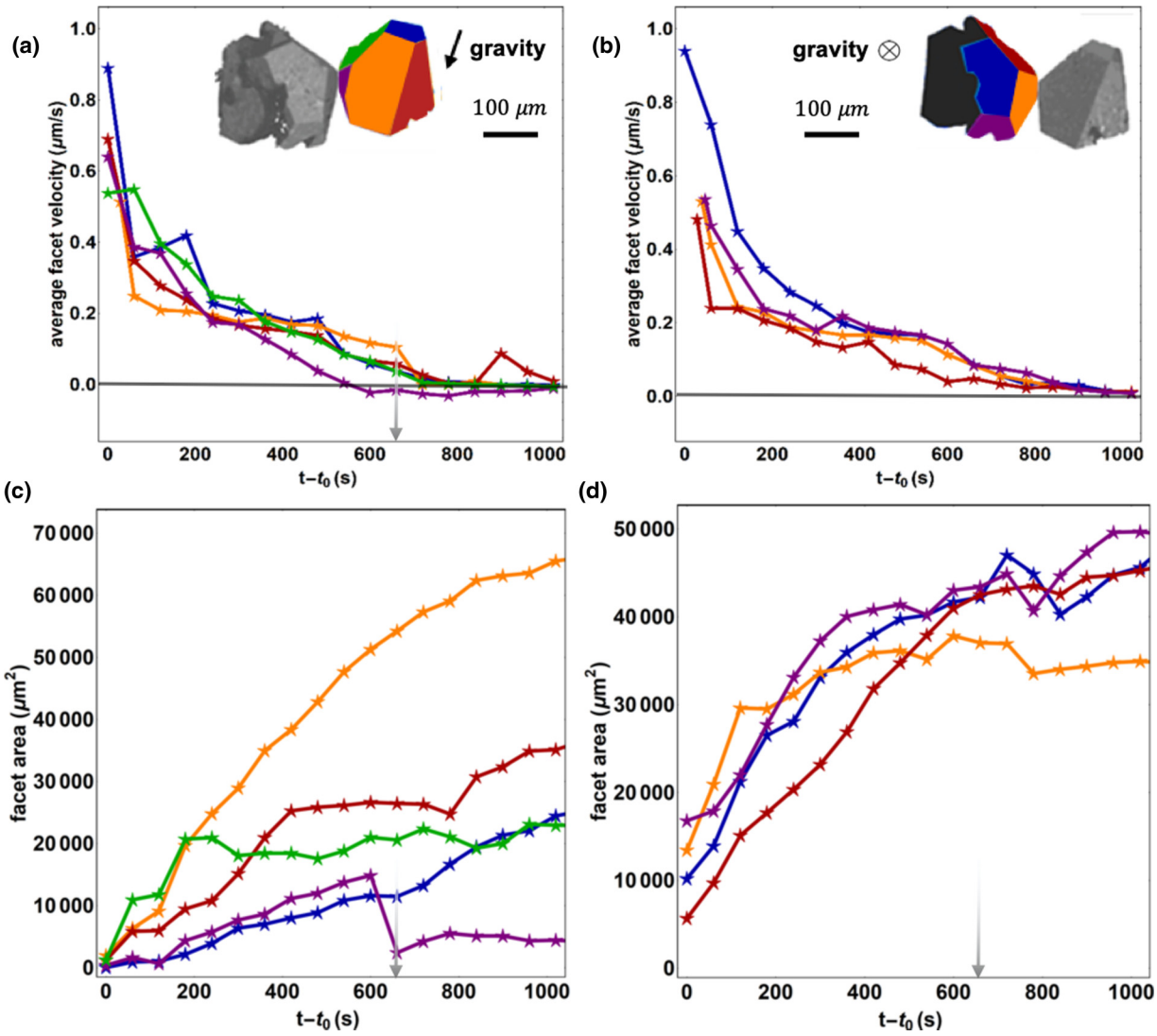

FIG. 4. *Local statistics on quasicrystal interactions*. (a) and (b) Facet velocities averaged over the QC surfaces and corresponding facet areas (c) and (d) as a function of time. (a) and (c) represent one QC, and (b) and (d) represent the other. The visible facets for each QC are color coded according to the dodecahedron shown inset. Errors in facet velocity measurements are ± 0.01 μm/s whereas errors associated with the facet area measurements are ± 0.05 μm^2 (not shown). As before, t_0 is the time at nucleation. The two QCs merge $\sim$700 s after nucleation (see the arrow), resulting in an abrupt change in the areas of the purple and orange facets in (c) and (d).

potential for the facet, which we take to be proportional to its weighted mean curvature K. It can be shown that the weighted mean curvature of a facet is inversely proportional to its length in two dimensions or area in 3D [51]. For a system with isotropic interfacial energy, K reduces to the mean interfacial curvature $2/R$ where R is the radius of a spherical particle. Since, in our case, the kinetic shape of an i-QC is a regular dodecahedron, all facets are pentagonal and, hence, crystallographically indistinct. This means that they should possess the same interfacial mobility M and Gibbs-Thomson coefficient Γ. Then, for a given chemical potential in the liquid $\langle\mu\rangle_f$, a facet's propensity to grow or recede is set by its weighted mean curvature in Eq. (2). Take, for instance, the purple (denoted p) facet that is analyzed above. By comparing Figs. 4(c) and 4(d), its area (and, hence, radius of curvature K^{-1}) is, at least, two times lower than that of the orange (o) facet on the neighboring QC. Thus, $\mu_{eq}(p) > \langle\mu\rangle_f > \mu_{eq}(o)$ for the former to fall back ($v_p < 0$) and the latter to grow out ($v_o > 0$), assuming that the two facets see the same liquid in the narrow channel that separates them. These results indicate that the anisotropic interfacial dynamics can be well described as motion by weighted mean curvature.

IV. CONCLUSIONS

Through synchrotron-based XRT, we have tracked in real time and in three dimensions the solidification dynamics of three i-QCs. The dodecahedral particles nucleate heterogeneously at the oxide skin of the sample and grow into the undercooled liquid. We find the orientation selection of the nuclei is a weak function of the QC-oxide interphase energy, in stark contrast to cubic crystals. At the later stages of solidification, the i-QCs interfere with each other *via* coarsening and coalescence. This behavior is well described by the general

evolution equation for interfacial area concentration. Despite the relatively high temperatures involved in this paper, the rates of surface-energy-driven interfacial motion are quite low as compared to metal dendrites. This result may stem from the structural similarity between solid and liquid, which, in turn, would lower the diffusion potential. Our work provides the necessary benchmark data needed to model the crystallization of complex intermetallics. Future work aims to relate our kinetic observations to the chemical order of the undercooled liquid.

ACKNOWLEDGMENTS

We are grateful to S. Moniri, C. Reese, M. Rahman, R. Bhattacharya, and I. Han from the University of Michigan for assisting in the XRT experiment. We express our thanks to X. Xiao and P. Shevchenko from Argonne National Laboratory for setting up the beam line and preparing sample holders. We acknowledge support from the U.S. Department of Energy (DOE), Office of Science, Office of Basic Energy Sciences, under Award No. DE-SC0019118. This work was supported, in part, by the American Association for University Women through the AAUW American Postdoctoral Fellowship. This research used resources of the Advanced Photon Source, a U.S. Department of Energy (DOE), Office of Science User Facility operated for the DOE Office of Science by Argonne National Laboratory under Contract No. DE-AC02-06CH11357.

APPENDIX: BARRIER FOR HETEROGENEOUS NUCLEATION

The shape of the critical nucleus sitting on a flat substrate is determined by both the crystal-melt interfacial tension as well as the crystal-wall interfacial tension. As we will see, the latter determines the volume of critical nucleus. A discussion of the orientation selection of heterogeneous nuclei assuming cubic and octahedral Wulff shapes is given by Refs. [28,30]. Here, we apply their theoretical framework by changing the nucleus shape to a pentagonal dodecahedron. The total Gibbs free energy of nucleation can then written as

$$\Delta G = -\frac{V_c}{\nu_c}\Delta\mu + \sum_{i=1}^{12}\gamma_i \Delta A_i, \tag{A1}$$

where V_c is the volume, ν_c is the specific volume of the QC, $\Delta\mu$ is the nucleation driving force, γ_i is the energy of broad fivefold facet i, and ΔA_i is the area of that same facet. Since all bounding facets have the same orientation, they should have the same surface free energy, and thus, the second term can be expressed more compactly as γS where $S = \sum_{i=1}^{12}\Delta A_i$ is the total surface area of a dodecahedron. The barrier for heterogeneous nucleation ΔG^*_{het} is then,

$$\Delta G^*_{\text{het}} = \frac{V^*_{c,\text{het}}\Delta\mu}{2\nu_c}, \tag{A2}$$

where we have used the fact that, in general, $S \propto V_c^{2/3}$ and $\frac{\partial G}{\partial V_c}|_{V_c^*} = 0$. The homogeneous nucleation barrier ΔG^*_{hom} follows a similar form as in Eq. (A2). The ratio of the two barriers can then be computed as

$$\frac{\Delta G^*_{\text{het}}}{\Delta G^*_{\text{hom}}} = \frac{V^*_{c,\text{het}}}{V^*_{c,\text{hom}}}, \tag{A3}$$

where $V^*_{c,hom}$ is the volume of the "isolated" nucleus (i.e., without a foreign substrate), and $V^*_{c,het}$ is that of the nucleus partially "buried" by the substrate. The latter is set by the Winterbottom construction [31], which relates the degree of burial (h) to an interfacial tension,

$$\frac{\gamma_{wc} - \gamma_{wm}}{h} = \text{const.}, \tag{A4}$$

where, as before, γ_{wc} is the interfacial tension between oxide wall (w) and crystal (c), γ_{wm} is that between wall and melt (m), and h is the distance between the crystal center (Wulff's point) to the oxide-QC interfaces. Negative h indicates the center is below the substrate surface; positive h indicates the converse. Note the energy terms γ_{wc}, γ_{wm}, and $\gamma_{wc} - \gamma_{wm}$ are notoriously difficult to measure experimentally. However, through Eqs. (A3) and (A4), we can determine how changes in $\gamma_{wc} - \gamma_{wm}$ influence h, $V^*_{c,het}$, and ultimately $\frac{\Delta G^*_{\text{het}}}{\Delta G^*_{\text{hom}}}$. We perform such a calculation on a critical i-QC nucleus with specific orientation, twofold, threefold, or fivefold symmetries in the upper direction (i.e., away from the oxide substrate). By fixing its volume and orientation, we sweep through different values of h and recalculate the nucleation barrier with the aid of Eq. (A3), see Fig. 2 of the main text.

[1] W. Steurer, Twenty years of structure research on quasicrystals. part I. pentagonal, octagonal, decagonal and dodecagonal quasicrystals, Z. Kristallogr.-Cryst. Mater. **219**, 391 (2004).

[2] A. I. Goldman and M. Widom, Quasicrystal structure and properties, Annu. Rev. Phys. Chem. **42**, 685 (1991).

[3] A. P. Tsai, Icosahedral clusters, icosahedral order and stability of quasicrystals–a view of metallurgy, Sci. Technol. Adv. Mater. **9**, 013008 (2008).

[4] K. Hayashida, T. Dotera, A. Takano, and Y. Matsushita, Polymeric Quasicrystal: Mesoscopic Quasicrystalline Tiling in ABC Star Polymers, Phys. Rev. Lett. **98**, 195502 (2007).

[5] C. R. Iacovella, A. S. Keys, and S. C. Glotzer, Self-assembly of soft-matter quasicrystals and their approximants, Proc. Natl. Acad. Sci. USA **108**, 20935 (2011).

[6] J. Mikhael, M. Schmiedeberg, S. Rausch, J. Roth, H. Stark, and C. Bechinger, Proliferation of anomalous symmetries in colloidal monolayers subjected to quasiperiodic light fields, Proc. Natl. Acad. Sci. USA **107**, 7214 (2010).

[7] D. Shechtman, I. Blech, D. Gratias, and J. W. Cahn, Metallic Phase with Long-Range Orientational Order and no Translational Symmetry, Phys. Rev. Lett. **53**, 1951 (1984).

[8] D. Shechtman and I. Blech, The microstructure of rapidly solidified Al_6Mn, Metall. Trans. A **16**, 1005 (1985).

[9] W. Steurer, Quasicrystals: What do we know? what do we want to know? what can we know?, Acta Crystallogr., Sect. A: Found. Adv. **74**, 1 (2018).

[10] V. Simonet, F. Hippert, M. Audier, and R. Bellissent, Local order in liquids forming quasicrystals and approximant phases, Phys. Rev. B **65**, 024203 (2001).

[11] J. Taylor, E. Teich, P. Damasceno, Y. Kallus, and M. Senechal, On the form and growth of complex crystals: The case of Tsai-type clusters, Symmetry **9**, 188 (2017).

[12] P. J. Steinhardt and H.-C. Jeong, A simpler approach to penrose tiling with implications for quasicrystal formation, Nature (London) **382**, 431 (1996).

[13] C. Beeli and H.-U. Nissen, Growth morphology of icosahedral Al-Mn-Pd single quasicrystals, Philos. Mag. B **68**, 487 (1993).

[14] C. Beeli, T. Godecke, and R. Luck, Highly faceted growth shape of microvoids in icosahedral Al-Mn-Pd, Philos. Mag. Lett. **78**, 339 (1998).

[15] J. Robertson, M. Misenheimer, S. Moss, and L. Bendersky, X-ray and electron metallographic study of quasicrystalline AlMnSi alloys, Acta Metall. **34**, 2177 (1986).

[16] B. Dubost, J. Lang, M. Tanaka, P. Sainfort, and M. Audier, Large AlCuLi single quasicrystals with triacontahedral solidification morphology, Nature (London) **324**, 48 (1986).

[17] F. W. Gayle, Free-surface solidification habit and point group symmetry of a faceted, icosahedral Al-Li-Cu phase, J. Mater. Res. **2**, 1 (1987).

[18] H. N. Thi, J. Gastaldi, T. Schenk, G. Reinhart, N. Mangelinck-Noel, V. Cristiglio, B. Billia, B. Grushko, J. Härtwig, H. Klein, and J. Baruchel, In situ and real-time probing of quasicrystal solidification dynamics by synchrotron imaging, Phys. Rev. E **74**, 031605 (2006).

[19] J. Gastaldi, G. Reinhart, H. Nguyen-Thi, N. Mangelinck-Noël, B. Billia, T. Schenk, J. Haertwig, B. Grushko, H. Klein, A. Buffet *et al.*, In situ study of quasicrystal growth by synchrotron x-ray imaging, Philos. Mag. **87**, 3079 (2007).

[20] I. Han, X. Xiao, and A. J. Shahani, Probing the growth and melting pathways of a decagonal quasicrystal in real-time, Sci. Rep. **7**, 17407 (2017).

[21] N. Senabulya, X. Xiao, I. Han, and A. J. Shahani, On the kinetic and equilibrium shapes of icosahedral Al_{71} Pd_{19} Mn_{10} quasicrystals, Scr. Mater. **146**, 218 (2018).

[22] I. Han, X. Xiao, H. Sun, and A. J. Shahani, A side-by-side comparison of the solidification dynamics of quasicrystalline and approximant phases in the Al-Co-Ni system, Acta Crystallogr., Sect. A: Found. Adv. **75** , 281 (2019).

[23] D. Gürsoy, F. D. Carlo, X. Xiao, and C. Jacobsen, TomoPy: A framework for the analysis of synchrotron tomographic data, J. Synchrotron Radiat. **21**, 1188 (2014).

[24] MATLAB, *version 7.14.0 (R2012a)* (The MathWorks Inc., Natick, MA, 2012).

[25] M. Botsch, L. Kobbelt, M. Pauly, P. Alliez, and B. Levy, *Polygon Mesh Processing* (A.K. Peters, Natick, MA, 2010).

[26] A. Shahani, E. Gulsoy, V. Roussochatzakis, J. Gibbs, J. Fife, and P. W. Voorhees, The dynamics of coarsening in highly anisotropic systems: Si particles in Al-Si liquids, Acta Mater. **97**, 325 (2015).

[27] A. J. Shahani, X. Xiao, K. Skinner, M. Peters, and P. W. Voorhees, Ostwald ripening of faceted Si particles in an Al-Si-Cu melt, Mater. Sci. Eng., A **673**, 307 (2016).

[28] M. Uwaha, Equilibrium crystal shapes on a flat substrate, Jpn. J. Appl. Phys., Part 1 **26**, 1592 (1987).

[29] J. E. Taylor and J. W. Cahn, Theory of orientation textures due to surface energy anisotropies, J. Electron. Mater. **17**, 443 (1988).

[30] K. Fujiwara, K. Maeda, H. Koizumi, J. Nozawa, and S. Uda, Effect of silicon/crucible interfacial energy on orientation of multicrystalline silicon ingot in unidirectional growth, J. Appl. Phys. **112**, 113521 (2012).

[31] W. Winterbottom, Equilibrium shape of a small particle in contact with a foreign substrate, Acta Metall. **15**, 303 (1967).

[32] R. Kaischew, Equilibrium shape and work of formation of crystalline nuclei on a foreign substrate, Commun. Bulg. Acad. Sci. **1**, 100 (1950).

[33] S. Marsh and M. Glicksman, Overview of geometric effects on coarsening of mushy zones, Metall. Mater. Trans. A **27**, 557 (1996).

[34] C. Wert and C. Zener, Interference of growing spherical precipitate particles, J. Appl. Phys. **21**, 5 (1950).

[35] M. Glicksman, K.-G. Wang, and S. Marsh, Diffusional interactions among crystallites, J. Cryst. Growth **230**, 318 (2001).

[36] T. Courtney and J. Lee, An analysis for estimating the probability of particle coalescence in liquid phase sintered systems, Metall. Trans. A **11**, 943 (1980).

[37] H. Neumann-Heyme, K. Eckert, and C. Beckermann, General evolution equation for the specific interface area of dendrites during alloy solidification, Acta Mater. **140**, 87 (2017).

[38] J. Cahn, Significance of average mean curvature and its determination by quantitative metallography, Trans. Metall. Soc. AIME **239**, 610 (1967).

[39] B. B. Rath, Kinetics of nucleation and growth processes, Mater. Sci. Eng., B **32**, 101 (1995).

[40] L. Ratke and P. W. Voorhees, *Growth and Coarsening: Ostwald Ripening in Material Processing* (Springer, Berlin/Heidelberg, 2013).

[41] D. R. Poirier, S. Ganesan, M. Andrews, and P. Ocansey, Isothermal coarsening of dendritic equiaxial grains in Al15.6wt.%Cu alloy, Mater. Sci. Eng., A **148**, 289 (1991).

[42] L. Ratke and C. Beckermann, Concurrent growth and coarsening of spheres, Acta Mater. **49**, 4041 (2001).

[43] N. Limodin, L. Salvo, E. Boller, M. Suéry, M. Felberbaum, S. Gailliègue, and K. Madi, In situ and real-time 3-D microtomography investigation of dendritic solidification in an Al-10 wt.% Cu alloy, Acta Mater. **57**, 2300 (2009).

[44] S. Shuai, E. Guo, A. Phillion, M. D. Callaghan, T. Jing, and P. D. Lee, Fast synchrotron x-ray tomographic quantification of dendrite evolution during the solidification of MgSn alloys, Acta Mater. **118**, 260 (2016).

[45] C. Kuehmann and P. W. Voorhees, Ostwald ripening in ternary alloys, Metall. Mater. Trans. A **27**, 937 (1996).

[46] K. F. Kelton, Quasicrystals: Structure and stability, Int. Mater. Rev. **38**, 105 (1993).

[47] M. Gündüz and J. Hunt, The measurement of solid-liquid surface energies in the Al-Cu, Al-Si and Pb-Sn systems, Acta Metall. **33**, 1651 (1985).

[48] M. Gündüz and J. Hunt, Solid-liquid surface energy in the Al-Mg system, Acta Metall. **37**, 1839 (1989).

[49] W. C. Carter, A. R. Roosen, J. W. Cahn, and J. E. Taylor, Shape evolution by surface diffusion and surface attachment limited kinetics on completely faceted surfaces, Acta Metall. Mater. **43**, 4309 (1995).

[50] A. R. Roosen and W. C. Carter, Simulations of microstructural evolution: Anisotropic growth and coarsening, Physica A **261**, 232 (1998).

[51] J. E. Taylor, II-mean curvature and weighted mean curvature, Acta Metall. Mater. **40**, 1475 (1992).